Journal of Zhejiang University-SCIENCE A 2025 26(10):967-982
www.jzus.zju.edu.cn; www.springer.com/journal/11582
E-mail: jzus_a@zju.edu.cn

Research Article
https://doi.org/10.1631/jzus.A2400235

Check for updates

Rail profile optimization through balancing of wear and fatigue

Binjie XU[1], Zhiyong SHI[2], Yun YANG[1], Jianxi WANG[3], Kaiyun WANG[1]✉

[1]*State Key Laboratory of Rail Transit Vehicle System, Southwest Jiaotong University, Chengdu 610031, China*
[2]*Department of Industrial Engineering, University of Florence, Florence, Italy*
[3]*School of Civil Engineering, Shijiazhuang Tiedao University, Shijiazhuang 050001, China*

Abstract: Rail profile optimization is a critical strategy for mitigating wear and extending service life. However, damage at the wheel-rail contact surface goes beyond simple rail wear, as it also involves fatigue phenomena. Focusing solely on wear and not addressing fatigue in profile optimization can lead to the propagation of rail cracks, the peeling of material off the rail, and even rail fractures. Therefore, we propose an optimization approach that balances rail wear and fatigue for heavy-haul railway rails to mitigate rail fatigue damage. Initially, we performed a field investigation to acquire essential data and understand the characteristics of track damage. Based on theory and measured data, a simulation model for wear and fatigue was then established. Subsequently, the control points of the rail profile according to cubic non-uniform rational B-spline (NURBS) theory were set as the research variables. The rail's wear rate and fatigue crack propagation rate were adopted as the objective functions. A multi-objective, multi-variable, and multi-constraint nonlinear optimization model was then constructed, specifically using a Levenberg Marquardt-back propagation neural network as optimized by the particle swarm optimization algorithm (PSO-LM-BP neural network). Ultimately, optimal solutions from the model were identified using a chaos microvariation adaptive genetic algorithm, and the effectiveness of the optimization was validated using a dynamics model and a rail damage model.

Key words: Heavy-haul railway; Rail wear; Rail fatigue; Levenberg Marquardt-back propagation neural network as optimized by the particle swarm optimization algorithm (PSO-LM-BP neural network); Rail profile optimization; Multi-objective optimization

1 Introduction

Imbalances in resource allocation and demand in China have prompted the development of heavy-haul railways with large capacity, low energy consumption, and high efficiency. This has enabled the Chinese rail system to carry 25% of the global railway transportation volume, with only 6% of the global operating mileage. However, with these large increases in railway transportation capacity, the risk of rail damage has become increasingly severe, posing challenges for maintenance and operational safety. In particular, severe wear and fatigue cracking problems in small-radius-curve rails are prominent (Zhai et al., 2014). Typical solutions for these issues include rail grinding and oil lubrication. Rail grinding can effectively remove surface impurities, while oil lubrication can control the coefficient of friction between the wheel and the rail, thus reducing material loss. However, excessive rail grinding can shorten the rail's service life and increase maintenance costs (Zhang et al., 2019). The oil lubricants can also enter cracks and accelerate their expansion under the action of the wheels on the rail (Zhao et al., 2021).

In response to the wear and fatigue issues of small-radius-curve rails in heavy-haul railways, the academic community has investigated and proposed various optimization strategies to mitigate rail damage. For instance, Kalousek et al. (1989) developed a preventive rail grinding strategy, which determined the necessary time of rail surface materials to induce initial cracks. They also found that multiple bouts of mild grinding could quickly restore the rail to an ideal profile and mitigate the initiation and propagation rate of cracks. Grassie et al. (2002) designed an optimized rail profile for the "Malmbanan" heavy-haul line and conducted a grinding experiment. Their results showed

✉ Kaiyun WANG, kywang@swjtu.edu.cn
Binjie XU, https://orcid.org/0009-0005-8671-1181
Kaiyun WANG, https://orcid.org/0000-0003-0958-4260

Received May 6, 2024; Revision accepted June 27, 2024;
Crosschecked July 15, 2025; Online first Sept. 18, 2025

that the optimized profile had a good matching state with the wheels, effectively reduced contact stress, and minimized the rolling contact fatigue cracks in the rail gauge area. Looking from a different angle, Wang et al. (2007) studied the causes of oblique cracks on the rail surface. They modified the contact point position between the wheel and the rail using an asymmetric grinding method, which reduced the contact stress and effectively controlled the rolling contact fatigue cracks. Magel and Kalousek (2002) optimized a curved rail profile based on the rolling radius difference (RRD). They performed field tests to validate the effectiveness of the optimized profile in mitigating rolling contact fatigue and wear.

By applying lubrication, Evans et al. (2008) optimized the conicity wheel and the rail profile, substantially reducing re-profiling intervals and improving running stability. Zhou et al. (2021) combined small-scale wheel-rail contact fatigue tests and finite element analysis to verify the coexistence of wear and rolling contact fatigue during the rail service life. In addition, Zhou et al. (2015) analyzed the relationships among rail gauge corner-rolling contact fatigue cracks, wear, and hardness, discovering that the development of gauge corner fatigue cracks occurred in three stages: rapid initiation of cracks, coexistence of cracks and wear, and control of cracks by the wear. Ding et al. (2012) obtained the distribution of normal stress, tangential stress, and maximum shear at different depths on the material surface in the contact patch by applying 3D elastic body non-Hertzian rolling contact theory. They analyzed the influence of the wheel material on the competitive relationship between wheel wear and fatigue. In an example pertaining to heavy-haul lines, Xie et al. (2023) investigated the oblique cracks of rail wear and fatigue on heavy-haul lines and found that increasing rail wear could significantly inhibit the development of fatigue cracks. Looking at curved rails again, Yang (2019) optimized the profile of a small radius of curved rail through numerical analysis and realized a balance between rail wear and cracking, effectively inhibiting the generation of rail surface cracks. Wang et al. (2015) used virtual prototypes to study the influence of curve parameters and track parameters on rail wear. They summarized these measures to optimize curve parameters, enabling the reduction of wear. Finally, Li et al. (2024) proposed new countermeasures for wheel and rail profile optimization, which were verified through field tests and increased vehicle operation safety.

In summary, wear and surface rolling contact fatigue in heavy-haul rails are intertwined, developing together under the continuous interaction of the wheels and the rail. Jointly, they determine the service life of the rail. They are also in a competitive relationship: when wear dominates, it will inhibit the expansion of surface fatigue cracks, and when fatigue dominates, the cracks will continue to deepen. Currently, optimizing the rail profile is an effective means of reducing rail wear. However, most studies have not fully considered the interaction between wear and fatigue, and their impact on failure mechanisms. Therefore, even if a seemingly optimal profile is found, it cannot be guaranteed that it will lead to the longest service life. For this reason, in this study, we develop a method for rail profile optimization that balances wear and fatigue.

2 Curve rail wear and fatigue damage characteristics

Heavy-haul railways are crucial for achieving efficient cross-country coal transport in China. In 2022, the total coal transport volume nationwide reached 4.786 billion tons, with heavy-haul railways carrying 2.900 billion tons, accounting for 58.3% of the total. This enormous transport volume has exerted pressure on heavy-haul lines. In this context, we conducted long-term tracking tests on the Shuo-Huang railway track to begin our study. Specifically, we analyzed the track damage characteristics to inform our thinking on potential maintenance strategies.

Pictures from our field study in Fig. 1a show that when the curve radius is less than 600 m, the main problem is rail wear damage and fatigue damage is of secondary importance. However, when the curve radius is more than 1000 m, rail fatigue damage gradually becomes the primary problem, and wear damage is secondary. Methods as shown in Fig. 1b were applied to measure rail wear, fatigue cracks, and vertical and lateral forces. The results of these measurements are shown in Figs. 1c–1f. Figs. 1c and 1d show that on a 600 m radius curve, rail wear of the gauge corner is predominant when the total railed tonnage is within 0 to 63 million tons (Mt). However, when the railed tonnage exceeds 63 Mt, rail side wear begins to develop.

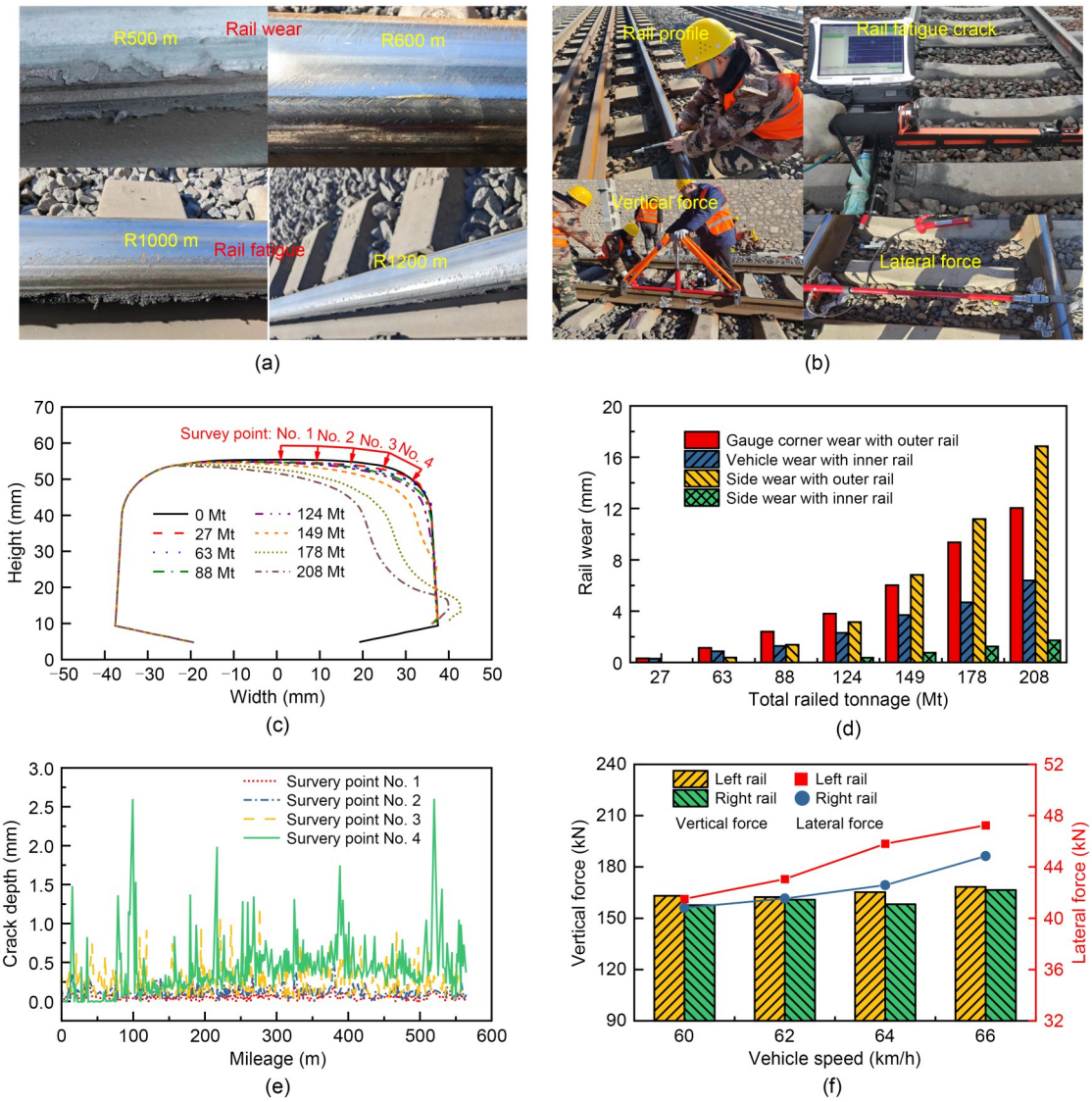

Fig. 1 Field investigation: (a) damage characteristics of the curve line; (b) investigation equipment; (c) variation law of rail wear; (d) rail wear test result; (e) rail fatigue crack; (f) wheel-rail lateral and vertical force. References to color refer to the online version of this figure

When the railed tonnage exceeds 149 Mt, side wear exceeds gauge corner wear, becoming the primary wear mechanism. When the railed tonnage is 208 Mt, the gauge corner wear on the outer rail is 12.03 mm, while the side wear increases to 16.8 mm.

For a total railed tonnage of 88 Mt, using the four-channel high-performance eddy current tester (Roman WPG-D340, Germany), we tested rolling contact fatigue (RCF) cracks at four positions on the R600 m radius curved rail, as shown in Fig. 1c. Fig. 1e measurement results show that the depth of fatigue cracks on the rail surface gradually increases from the top surface heading to the gauge corner area, with measuring point No. 1 having minor fatigue crack depth of only 0.38 mm. The crack depth at measuring point No. 4 is 2.64 mm. These results, in combination with dynamic simulations, finite element calculations, and the energy index method, can be used to determine the amount of fatigue damage of the rail and predict the fatigue crack propagation depth in the rail. Fig. 1f shows the results of the wheel-rail force. The data indicates that when vehicles travel at speeds of 60–66 km/h along curves, the lateral and vertical forces on the outer rail are greater than those on the inner rail. The maximum vertical forces on the inner and outer rails are 166 and 168 kN, respectively, while the maximum lateral forces on the inner and outer rails are 44.8 and 47.2 kN, respectively.

3 Curve rail wear and fatigue damage characteristics

Rail wear and contact fatigue are two key factors determining the service life of heavy-haul rails, both of which originate from microscopic damage to the rail contact surface. These damages gradually develop on the wheel-rail contact surface, leading to macroscopic wear and fatigue phenomena. It is worth noting that the calculations of rail wear and rolling contact fatigue cracks are based on wheel-rail forces. Still, these two phenomena are often difficult to distinguish at the microscopic level. To accurately understand these two phenomena, this study delves into the microscopic changes and mechanisms present in the wheel-rail contact process.

3.1 Rail wear

Rail wear refers to the phenomenon in which the surface materials of the wheel and rail continuously wear down, due to mechanical or chemical actions during their relative movement (Wang and Gao et al., 2015). This phenomenon leads to surface wear on the wheel and rail, alters their profiles, and consequently affects their contact relationship. Common material wear models used in rail wear calculations include the Archard (Challen et al., 1986), Specht (Kang et al., 2002), and VNIIZHT models (Zakharov et al., 2008). The Archard model is often used to analyze rolling contact and sliding problems. This model suggests that the primary reason for rail wear is the magnitude of the contact stress at the rail-wheel interface, caused by the work of rolling or sliding forces between the wheel and rail. According to the model, the volume of material wear is related to the normal contact force and the sliding distance between the wheel and the rail.

The Archard wear theory and the calculation method for wheel-rail creep rate are shown in the electronic supplementary materials.

According to Kalker (1982)'s simplification theory, the wheel–rail contact patch is divided into several cells, as shown in Fig. 2. The length and width of the cells are dx and dy, respectively. The wear depth of any cell in the contact spot is:

$$\Delta V_{\mathrm{w}}=k_{\mathrm{w}}\frac{F_{zi}}{H}\Delta x\sqrt{(\xi-\phi y_i)^2+(\eta-\phi x_i)^2}, \quad (1)$$

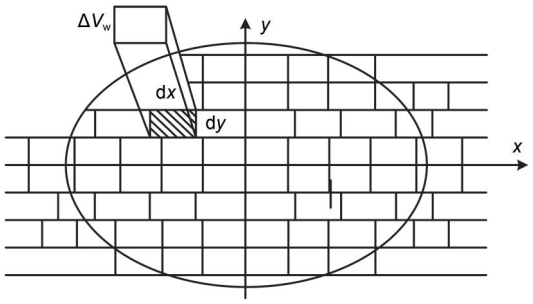

Fig. 2 Discretization of the contact patch

where k_{w} is the wear coefficient, F_{zi} is the normal contact stress in unit i of the contact patch, H is the material hardness, and ξ, η, and ϕ are the longitudinal, transverse, and spin creep rates of the wheel. The spin creep rate describes the velocity characteristic of the wheel rotating around an axis perpendicular to the contact patch plane when the wheel is in contact with the rail, which results in slight relative sliding within the contact patch. x_i and y_i are the transverse and longitudinal coordinates of unit i of the contact patch, respectively.

The wear coefficient k_{w} and the normal force F_{zi} are the critical parameters for calculating the wear depth of any point in the contact patch. According to Jendel (2002)'s theory, the value of the wear coefficient k_{w} depends on the sliding distance and the normal force. Based on the severity of wear, the wear coefficient is divided into four regions, as shown in the upper left corner of Fig. 3. Wear may lead to two or more points of contact between the wheel and rail, a scenario not describable by Hertz's contact theory. Instead, the Kik-Piotrowski (KP) multiple-point contact algorithm is more stable in calculating abnormal fluctuations in wheel and rail curvature (Sun et al., 2018). It also offers higher precision in determining the normal force between the wheel and the rail. The KP theory of contact can be used to determine:

$$F_{zi}=\frac{\pi E\delta_0}{2(1-\mu^2)}\frac{\int_{y_{\mathrm{r}}}^{y_{\mathrm{l}}}\int_{-x_{\mathrm{l}}(y)}^{x_{\mathrm{l}}(y)}\sqrt{x_{\mathrm{l}}^2(y)-x^2}\,\mathrm{d}x\mathrm{d}y}{\int_{y_{\mathrm{r}}}^{y_{\mathrm{l}}}\int_{-x_{\mathrm{l}}(y)}^{x_{\mathrm{l}}(y)}\sqrt{\dfrac{x_{\mathrm{l}}^2(y)-x^2}{x^2+y^2}}\,\mathrm{d}x\mathrm{d}y}, \quad (2)$$

$$\delta=(v_{\mathrm{w}}-v_{\mathrm{r}})\boldsymbol{n},$$

where μ is Poisson's ratio, E is Young's modulus, and δ is the penetration speed. Subscripts l and r denote the positions of the two sides of the contact patch in

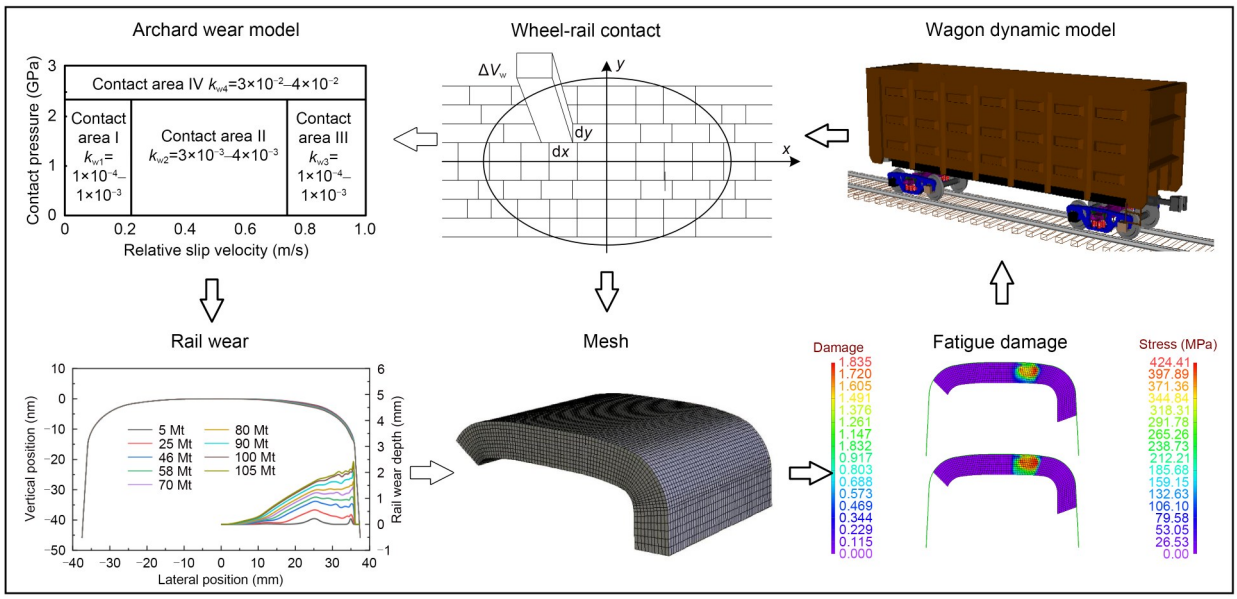

Fig. 3 Calculation process of rail rolling contact fatigue. References to color refer to the online version of this figure

the coordinate system, x_l and x_r denote the boundary positions of the contact patch in the lateral direction, while y_l and y_r represent the boundary positions of the contact patch in the longitudinal direction. v_w and v_r are the speeds of the wheel and rail at the contact point, and $\boldsymbol{n}$ is the normal vector at the contact point. The KP set δ_0=0.55δ.

3.2 Rail contact fatigue

Rolling contact fatigue of rail occurs due to cyclical loading of the wheel and rail, which generates significant shearing stress in the surface or body of the rail, causing plastic flow in the material (Xu et al., 2023). When the plastic flow exceeds the deformation limit of the material, fatigue cracks are generated. These cracks then gradually develop, leading to rail peeling, fractures, and other defects, which can potentially cause serious accidents if left untreated.

3.2.1 Rolling contact fatigue crack prediction

Current research commonly utilizes stability diagrams (Ekberg and Marais, 2000) and damage functions (Hiensch and Burgelman, 2019) to describe rail fatigue. These methods enable quantitative analysis of the mechanism and potentiality of RCF cracks. However, they cannot predict the development of rail cracks. Therefore, in this study, we employ the finite element method to calculate crack damage values, integrating field-measured crack data to establish a relationship between the depth of rolling contact fatigue cracks and fatigue damage values (Eq. (3)), thus enabling the prediction of rail crack development. The steps for calculating crack damage are illustrated in Fig. 3. First, a model for the interaction between vehicles and tracks and a model for wheel-rail wear are developed to calculate the rail profile after each wear iteration. Second, using the CONTACT program, the wheel-rail forces and creep rates under different wear profiles are simulated, and these results are incorporated into the rail finite element model. Lastly, the damage accumulated at grid nodes is distributed to newly constructed nodes using interpolation methods, and the process of accumulating RCF damage is repeated at the rail's new finite element grid nodes.

$$h=\frac{Qh_s}{Q_s}, \tag{3}$$

where h_s is the measured rail crack depth and Q_s is the measured fatigue damage value. By calculating the fatigue damage value Q of the rail surface through simulation, the crack depth h of the rail surface can be obtained for a given total railed tonnage M.

3.2.2 Wheel-rail contact stress model

The simplest criterion used in the simulation of RCF damage accumulation is the amplitude of maximum shear stress t_{max} (Zakharov and Goryacheva,

2005). This criterion accounts for the stresses caused by normal and tangential tractions in the contact. However, it does not consider hydrostatic pressure, which plays an essential role since favorable conditions for forming and developing cracks are created when there is multiaxial tension in the material. In contrast, the formation of cracks is more difficult when there is multiaxial compression (You et al., 2022).

The equivalent stress distribution of the contact attachment region was analyzed by using the parallelepiped finite element model. The calculation process for equivalent stress at different node positions can be found in the electronic supplementary materials (ESM).

3.2.3 Fatigue damage calculation

The fatigue damage of heavy-haul railway rails can be considered as high-cycle fatigue. The stress for fatigue failure due to rail contact fatigue and the number of fatigue failure cycles should therefore satisfy the following equation:

$$N = C\sigma_{\mathrm{eq}}^{-m}, \tag{4}$$

where σ_{eq} is the stress state in the contact region, N is the number of variable stress cycles before the appearance of fatigue cracks, and C and m are the material correlation constants.

Building a predictive model for rail fatigue crack depth requires determining the material parameters C and m. The rail used on the Shuo-Huang heavy-haul railway is made of U78CrV material (Xu et al., 2024), with mechanical performance parameters detailed in Table 1.

Table 1 Material parameters of the heavy-haul rail

Parameter	Value	Parameter	Value
Rail density (kg/m)	78	Poisson's ratio	0.3
Friction coefficient	0.35	Tensile strength (MPa)	1080
Side wear coefficient	0.15	Young's modulus (MPa)	2.1×10^5

According to Miner's linear fatigue damage theory, the fatigue damage value Q on the rail surface is:

$$Q = \sum_{o=1}^{N_{\mathrm{it}}} \sum_{i=1}^{N_{\mathrm{exp}}} \sum_{j=1}^{N_i} \frac{M_{\mathrm{it}}}{M_{\mathrm{s}} N_i} a_i \frac{1}{N_n(j)}, \tag{5}$$

where N_{it} represents the number of iterations for simulating rail profile wear, N_{exp} is the number of numerical experiments, N_i denotes the loading cycle number for the ith numerical experiment, M_{it} is the tonnage allocated to each wear iteration, M_{s} is the mass calculated through the section, a_i represents the weight of the ith numerical experiment, and $N_n(j)$ signifies the number of fatigue failure cycles.

3.3 Dynamic modeling and model validation

The C80 freight car is a wide vehicle used on China's heavy-haul railways, with the topological structure shown in Fig. 4a. M_{wc} is the mass of the car body, I_{wcy} is the moment of inertia of the car body about the Y-axis through its center of mass, β_{wc} is the pitching angle, K_{wpz} is the primary vertical stiffness, C_{wpz} is the primary vertical damping, K_{wsz} is the secondary vertical stiffness, and C_{wsz} is the secondary vertical damping. It features a traditional three-piece bogie, consisting primarily of a body, side frames, wheelsets, and bolsters, among 11 rigid bodies, as shown in Fig. 4b. When modeling in the software, the body is considered to have six degrees of freedom (DOFs) (Hu et al., 2025), the bolster is only considered for its yaw DOF, the side frames for five DOFs (excluding side roll), and the wheelsets for six DOFs, resulting in a total of 42 DOFs for the model of the vehicle. The methods for considering other structures of the wagons can be found in the ESM.

Tian et al. (2009) and Yang et al. (2024) have pointed out that there is a mutual influence between connected heavy-haul train cars, especially when there is longitudinal impulsion between trains. Therefore, this study establishes a three-vehicle train model consisting of one locomotive pulling two freight cars. The vehicle is connected by 13A couplers, with the structure, buffer characteristics, coupler model considerations, and train model of the 13A coupler being detailed in Fig. 4c, where $f_{\mathrm{l}}(x)$ denotes the loading curve of the coupler buffer, $f_{\mathrm{u}}(x)$ denotes the unloading curve of the buffer, K_{buf} is the stiffness of the buffer, C_{buf} is the damping of the buffer, and K_{s} is the stiffness of the coupler structure. In the model, the rail is considered a rigid body, and equivalent lumped parameters are used to simulate the stiffness and damping of the subgrade structure beneath the rail. In the vehicle model, the wheel adopts Levenberg-Marquardt (LM) profile, and the rail adopts CHN75 profile. The gauge is 1435 mm, the rail bed slope is 1/40, and the wheel-rail friction coefficient is 0.3 (Wang et al., 2015). In dynamic simulations, the KP contact algorithm is used

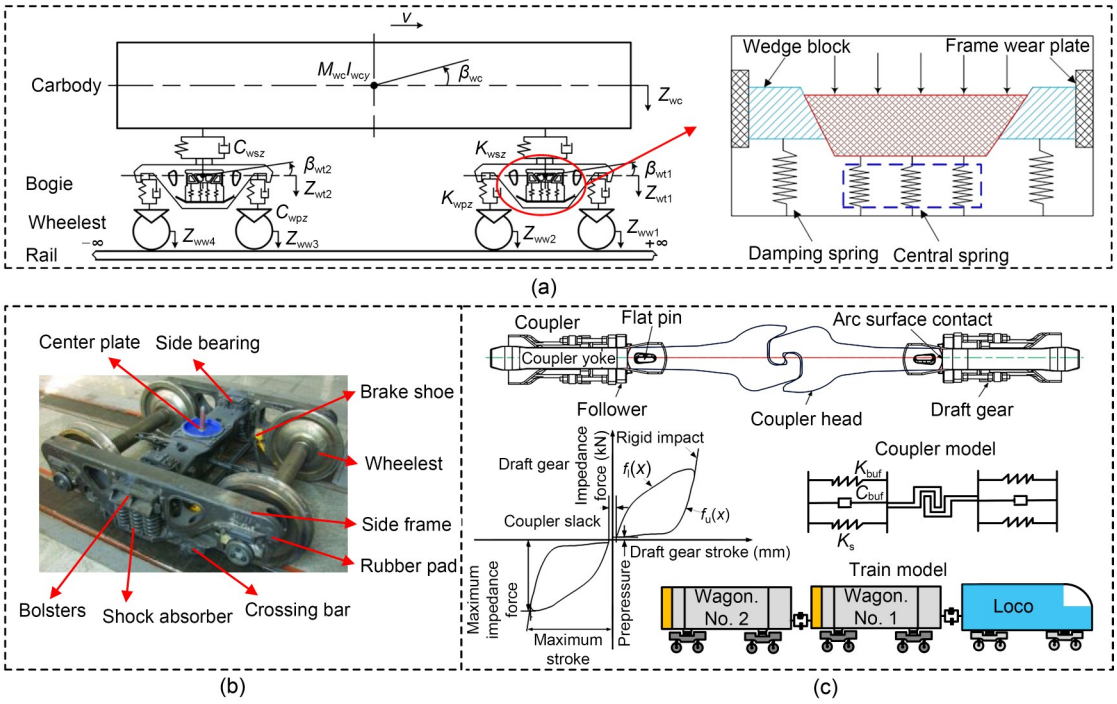

Fig. 4 Dynamic model of heavy-haul train: (a) vehicle model; (b) bogie model; (c) Coupler model

for normal contact calculation, and the FASTSIM algorithm is used for tangential contact calculation. Track irregularities are also made based on our measured data from the Shuo-Huang railway.

The wear calculation and dynamic models established in this section are validated by the field test on the Shuo-Huang heavy-haul railway. The verification process is shown in the ESM.

4 Multi-objective optimization for the rail profile

4.1 Description of the rail profile

The CHN75 rail profile is a continuous curve comprised of seven arcs and two straight segments. The non-uniform rational B-spline (NURBS) curve-fitting method offers flexibility, control, local adjustability, and strong convexity (Lin et al., 2021). By modifying the weight factors of the control points, the curvature can be controlled to meet the requirements of smoothness and continuity in profile fitting. After testing, the computational performance of the cubic NURBS curve was deemed to be the best and was used to fit the optimized rail profile. The derivation of the NURBS curve-fitting method and the cubic NURBS curve can be found in the ESM.

Based on the characteristics of the rail profile curve, a method that positively correlates with curvature is next employed to select the profile value points. The fixed coordinates and weight factors of the control points for the spline curve are integrated through reverse engineering, with the following steps:

(1) Determine the number of type value points

A discretization sampling method is adopted for the rail cross-axis X=[−36, 36] mm curve. When selecting points, consideration is given to the characteristics of the NURBS finite value points that describe complex curves. The analysis is conducted on the rail profile curve by selecting 20, 24, and 28 value points, respectively, for testing the appropriate number of value points.

(2) Determine the weight factors of the type value points

The importance of type value points with the curve is reflected by their weight factors. A higher weight factor indicates that the point significantly impacts the rail profile, and vice versa. Since the gauge angle region is substantial for wheel-rail matching, we refer to empirical formulas (Lin and Hu, 2020), and the weight factors of the value points within the

gauge angle region X=[23, 34] mm at the working edge of the rail are accordingly set to [0.9, 1.0]. The weight factors for the remaining parts of the value points are set to [0.5, 0.7].

According to empirical formulas, when fitting the CHN75 rail profile, three methods of selecting value points with counts of N=20, 24, and 28, respectively, are used. The effectiveness of these three methods is judged by the curve fitting correlation coefficient C_{rail}. The results of the three calculations are shown in Table 2.

Table 2 NURBS curve fitting correlations

Option	Number of type value points	C_{rail}
1	20	0.87
2	24	0.93
3	28	0.96

The results in Table 2 demonstrate that the greater the number of value points, the closer the interpolated curve is to the original curve. However, it also leads to higher computation time and cost. After considering the accuracy and computational efficiency, N=24 value points are selected for interpolation fitting. The CHN75 rail profile and its reconstructed profile are shown in Fig. 5.

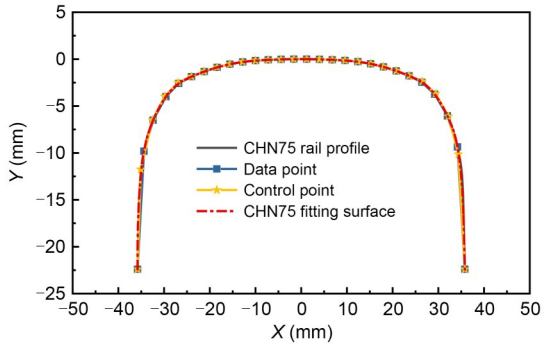

Fig. 5 Rail profile comparison

4.2 Multi-objective optimization model

4.2.1 Optimized variable design

Based on the results from Section 3.1, the reconstruction of the CHN75 rail profile using 24 type value points in a cubic NURBS curve is accurate and efficient. In the initial service stage of the curved outer rail of the heavy-haul railway, there is no change in the unworn profile within the [−36, 0] interval, while wear occurs in the [0, 36] mm area, and 12 type value points are sufficient to describe the worn profile. Therefore, the longitudinal coordinate y_i (i=1, 2, ⋯, 12) is set as a design variable in the optimization model.

4.2.2 Objective functions

The fatigue crack propagation rate k and the wear rate r are indicators used to evaluate the formation of rail wear and fatigue, and these two factors are naturally in competition. The development of wear can lead to a decrease in the rail's service life. At the same time, the expansion of fatigue cracks may result in rail fracture, posing a threat to operational safety. Therefore, we must ensure that the wear rate is greater than or equal to the crack propagation rate. The optimization objective for this goal is expressed as:

$$\min:\begin{cases} f_1=\max(|r_i|), \\ f_2=\max(|k_i|), \\ f_1\geqslant f_2, \end{cases} \tag{6}$$

where r_i is the rail wear rate at the ith measuring point, and k_i is the crack growth rate at the ith measuring point.

The objective function is normalized to a dimensionless function with the same order of magnitude as the variable, to ensure calculation accuracy. w_1 and w_2 represent the corresponding weight coefficients, with a constraint on the plane that $w_1+w_2=1$, and $w_1\geqslant w_2$. By building weight coefficient training models to simulate the multi-objective function, we determined that $w_1\geqslant 0.52$.

4.2.3 Constraints

The goal of optimizing the rail profile is to reduce wear damage. Therefore, the optimization design must meet the following requirements:

(1) The curve monotonicity of the rail profile is satisfied as:

$$\begin{cases} g[f_g'(y_i)<0], & i\in\{1,2,\cdots,12\}, \\ g[f_g'(y_i)>0], & i\in\{13,14,\cdots,24\}, \end{cases} \tag{7}$$

where $f_g(y_i)$ is the optimized profile curve equation under the ordinate of type value point i, and $f_g'(y_i)$ is the first derivation of the optimized profile curve equation.

(2) Constraint condition of concavity of rail profile curve:

$$g[f_g''(y_i)] \geqslant 0, \quad i \in \{1, 2, \cdots, 24\}, \tag{8}$$

where $g[f_g''(y_i)]$ is the second derivative of the optimized profile curve.

(3) The horizontal coordinate of the optimized profile should be lower than the horizontal coordinate prior to optimization.

(4) The optimized rail profile should ensure that safety indices such as derailment coefficient, wheel load reduction rate, wheelset lateral force, and overturning coefficient adhere to laws and regulations.

4.2.4 Levenberg Marquardt-back propagation neural network as optimized by the particle swarm optimization algorithm (PSO-LM-BP) neural network

The LM algorithm combines the features of gradient descent (local convergence) and the Gauss-Newton numerical optimization algorithm (global optimality) to achieve rapid global convergence (Zhao et al., 2007; Ran et al., 2023). Therefore, the LM-BP neural network significantly improves the convergence speed of the network and avoids the constraint of only being able to update in the direction of a negative gradient. More details on the concepts of a BP neural network and the LM algorithm can be found in the ESM.

In the process of PSO for LM-BP, the optimal position X of the particle is the weight and threshold obtained after optimization. The fitness function is chosen to be the mean squared error, shown in Eq. (9). The smaller the fitness value is, the more accurate the training will be.

$$F = \frac{1}{N}\sum_{i=1}^{N}\sum_{j=1}^{M}\left(y_{ij} - \bar{y}_{ij}\right)^2, \tag{9}$$

where N is the number of samples, M is the particle dimension, y_{ij} is the predicted value of the ith sample at the jth output network node, and $\bar{y}_{ij}$ is the actual value of the ith sample at the jth output network node.

Based on the PSO-LM-BP neural network, a multi-objective, multi-variable, and multi-constraint nonlinear optimization model for rail profiles is established. The control points of the rail profile are considered the independent variables $y=\{y_1, y_2, y_3, \cdots, y_n\}$, the rail wear rate r and fatigue crack propagation rate k are the objective functions, and the geometric characteristics of the rail and the vehicle's operational characteristics are the constraint conditions. The constraint condition is given by

$$\begin{cases} y = \{y_1, y_2, y_3, \cdots, y_n\}, \\ F = (r, k) \to \min, \\ \begin{cases} g[f_g'(y_i) < 0], & i \in \{1, 2, \cdots, 12\}, \\ g[f_g'(y_i) > 0], & i \in \{13, 14, \cdots, 24\}, \end{cases} \end{cases} \tag{10}$$

where y_1 to y_{n-1} represent the vertical coordinates of the 12 control points, and y_n denotes the total railed tonnage. The wear rate r is the ratio of the rail wear in the gauge angle region to the total railed tonnage, measured in mm/Mt. Similarly, the crack propagation rate k is the ratio of the crack growth at the gauge angle to the railed tonnage, also measured in mm/Mt.

4.3 Solution method

The ant colony optimization algorithm, simulated annealing algorithm, and genetic algorithm are among the most effective methods for solving nonlinear problems. The selection of parameters for the ant colony and simulated annealing algorithms often relies on empirical knowledge, leading to inconsistent results. The genetic algorithm is well known for its ability to avoid local optima and performs well in solving nonlinear problems (Nikbakht et al., 2021). Based on this, we adopted a modified genetic algorithm approach, which involved adding chaotic disturbances to the selection operator, adaptively adjusting the crossover and mutation operators, and improving the fitness function. This amplifies the advantages of the genetic algorithm and improves its evolutionary speed and search progress. The concept of microvariation, adaptive mutation operator, and chaotic disturbance are described further in the ESM.

The process is then applied to an R600 m curve of the Shuo-Huang railway. The technical route is shown in Fig. 6. The specific optimization steps include:

Step 1: Through field research and tracking tests, we accumulate a large amount of data on the fatigue and wear damage of heavy-haul tracks, laying a foundation for subsequent work.

Step 2: The theoretical calculation methods of wear and fatigue damage are introduced, and a C80 freight car model is established in the multi-body dynamics software UM using parameters specific to C80.

Step 3: A multi-objective optimization model is established based on the BP neural network using the

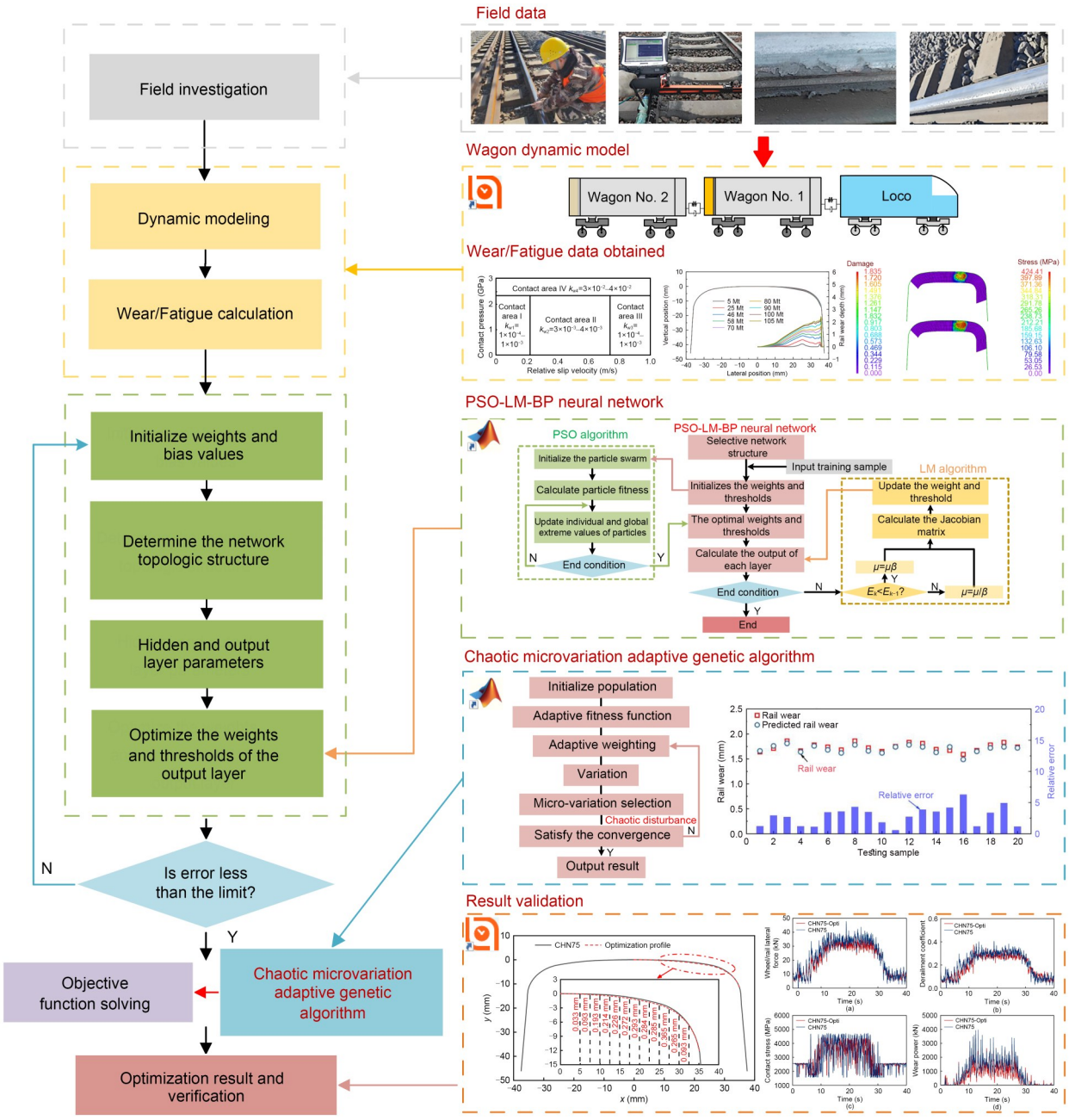

Fig. 6 Schematic diagram of rail profile optimization. References to color refer to the online version of this figure

PSO-LM algorithm, and our modified chaotic micro-variable adaptive genetic algorithm is introduced. Through the joint use of MATLAB and the UM software, this approach is used to solve the multi-objective optimization model and obtain an optimized profile that can reduce wheel-rail wear and fatigue.

Step 4: Based on the established vehicle dynamic model and wear model, we analyze the dynamic performance and wear and fatigue damage characteristics of the optimized profile, thus verifying the performance.

4.4 Rail optimization profile

Through the chaos microvariation adaptive genetic algorithm, an optimized rail profile that balances the wear and fatigue relationship for a curve with a radius of R600 m was successfully obtained, as shown in Fig. 7. Compared to the traditional profile, the optimized profile primarily shows improvements in the range of [5, 36] mm. Fig. 7 illustrates the grinding amounts required at every 2.5 mm interval; by

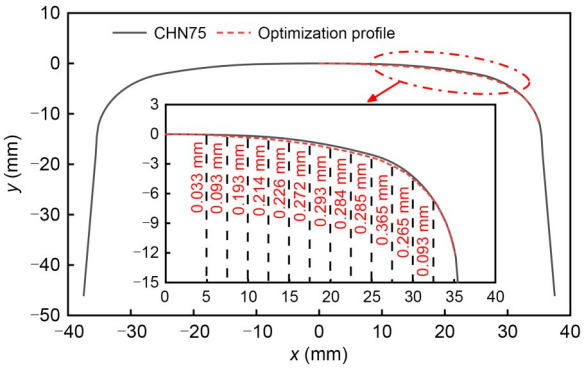

Fig. 7 Rail optimization profile

implementing such rail grinding operations, this optimized rail profile may be achieved. The position corresponding to the maximum grinding amount is at the abscissa of 27.5 mm, with a grinding amount of 0.365 mm.

5 Optimization of profile performance analysis

Section 4 demonstrated the application of optimized design methods and the leveraging of real conditions of the Shuo-Huang heavy-haul railway, to develop an optimal rail profile that can reduce wear and fatigue for an R600 m radius curve. Next, this section uses established vehicle dynamic models and fatigue damage models to test the dynamic behavior and damage status of the optimized profile.

5.1 Static wheel-rail mechanics

The wheel-rail contact characteristics, rolling radius difference, and equivalent conicity are vital parameters that define the wheel-rail surface matching relationship. These parameters are also significant for vehicle safety. The space trace method is used to calculate the contact relationship between the wheel and the optimized rail profile. Figs. 8a and 8b depict the distribution of the wheel-rail contact points. The contact area distribution of CHN75-Opti is larger and more uniform than that of CHN75, which helps prevent the concentration of stress at the contact points and reduces rail wear. The equivalent conicity shown in Fig. 8c indicates that within the lateral displacement range of 1 to 6 mm, the equivalent conicity of the CHN75 profile decreases. At the same time, the cone angle of CHN75-Opti remains relatively constant. Beyond a lateral displacement of 6 mm, both

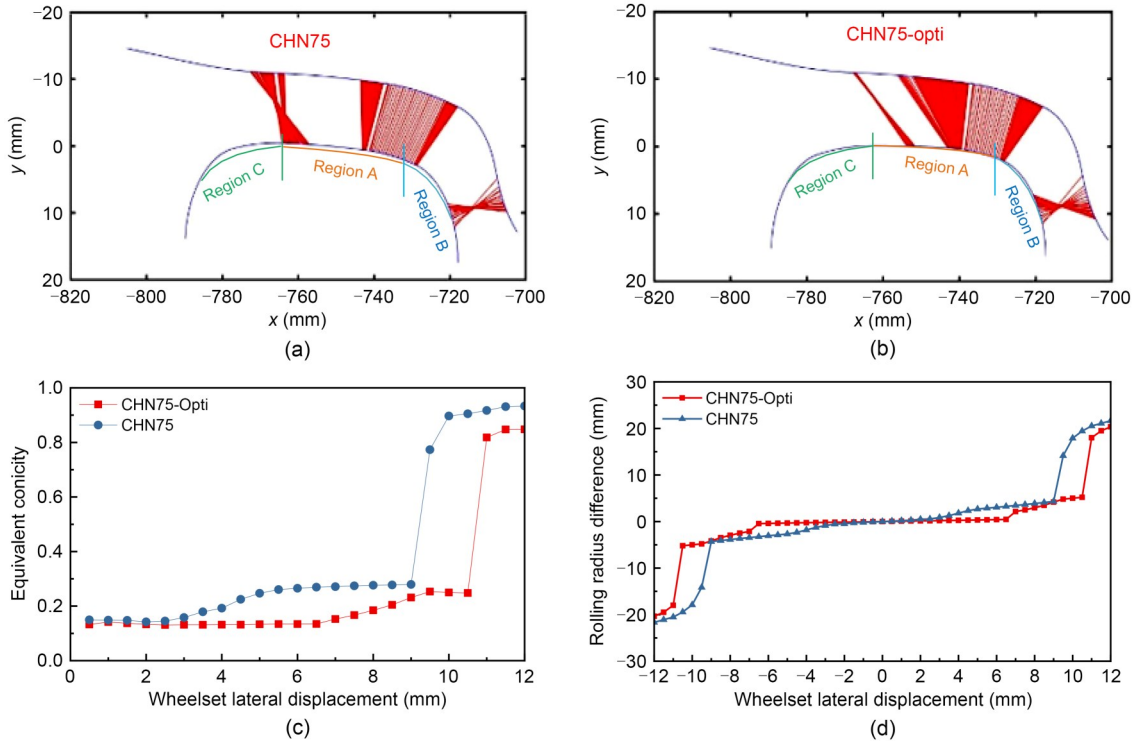

Fig. 8 Wheel-rail interaction investigations: (a) CHN75 with LM contact point pairs; (b) CHN75-Opti with LM contact point pairs; (c) equivalent conicity; (d) rolling radius difference

the CHN75 and CHN75-Opti profiles show a continuous increase in equivalent conicity, with respective maximum values of 0.93 and 0.84. Analysis of the wheel rolling radius difference in Fig. 8d reveals that the difference between the profiles is insignificant within a lateral displacement of 0 to 8 mm. When the lateral displacement is more than 8.5 mm, the wheel rolling radius difference for the CHN75 profile increases significantly instead. The CHN75-Opti profile also drastically changes after a lateral displacement exceeding 10.5 mm.

5.2 Dynamic results

Utilizing the established vehicle dynamics model, the dynamic performance of the C80 freight car was evaluated as shown in Fig. 9. Fig. 9a illustrates the influence of the optimized rail profile on the wheelset lateral force. When traversing a curve with a radius of R600 m on a CHN75 rail, the maximum wheelset lateral force was 47.7 kN. In contrast, using the CHN75-Opti profile under the same conditions, the maximum wheelset lateral force was reduced to 40.5 kN, a decrease of 15%. Fig. 9b shows the variation of the derailment coefficient. The use of the optimized profile reduced the maximum derailment coefficient from 0.41 to 0.36, a decrease of 10%. Fig. 9c presents the wheel-rail contact stress. The adoption of the optimized profile reduced the maximum wheel-rail contact stress from 4720 to 4251 MPa, again a decrease of 10%. Fig. 9d depicts the wear power. Using the optimized profile decreased the maximum wear power from 3936 to 2889 kN·m^2, or a reduction of 26.6%. These results indicate that operating heavy-haul vehicles on the CHN75-Opti rail can improve vehicle safety and reduce wheel-rail wear.

5.3 Rail wear and RCF damage

We next utilize the rail wear model and fatigue model to analyze the damage characteristics of the optimized rail, as shown in Fig. 10a. The maximum fatigue contact stress of the C80 freight car when matched with the CHN75 rail is 419.2 MPa, which reduces to 332.4 MPa (a 20.7% decrease) when matched with the CHN75-Opti rail. The contact area also appears to be increased. Fig. 10b indicates that the maximum damage accumulation for the C80 freight car is 0.175 when matched with the CHN75 rail and is reduced to 0.11 (a 37% decrease) when matched with the CHN75-Opti rail, showcasing a significant reduction in internal rail damage. Fig. 10c shows the cumulative

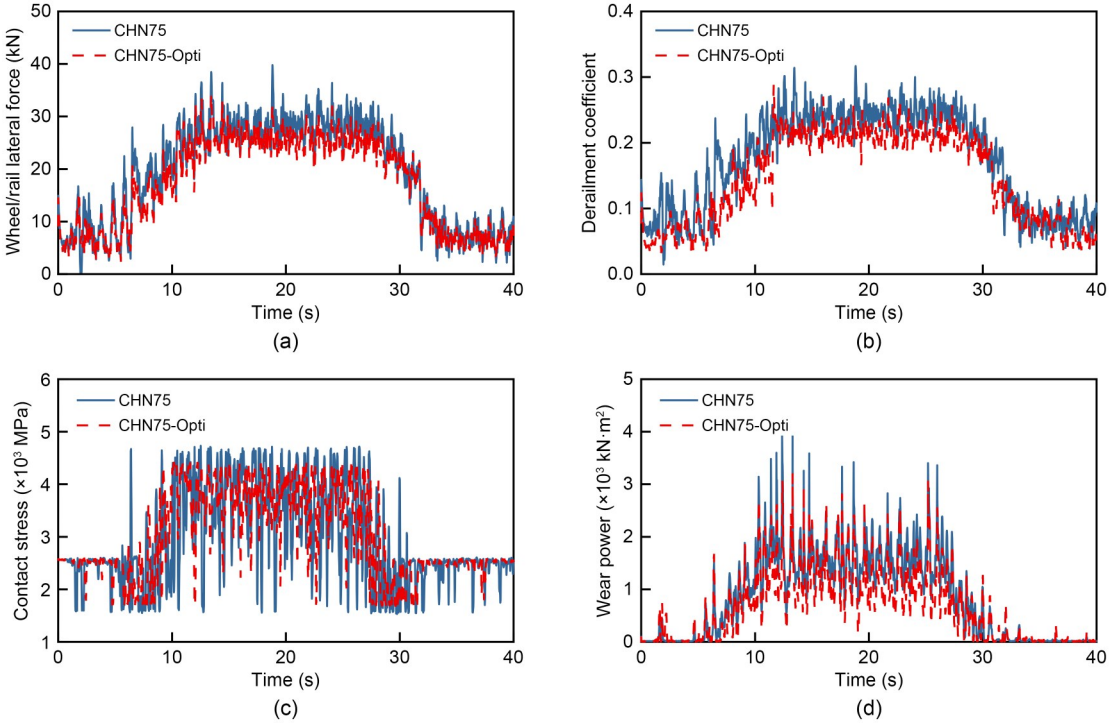

Fig. 9 Vehicle dynamic performance: (a) wheel/rail lateral force; (b) derailment coefficient; (c) wheel-rail contact stress; (d) rail wear power

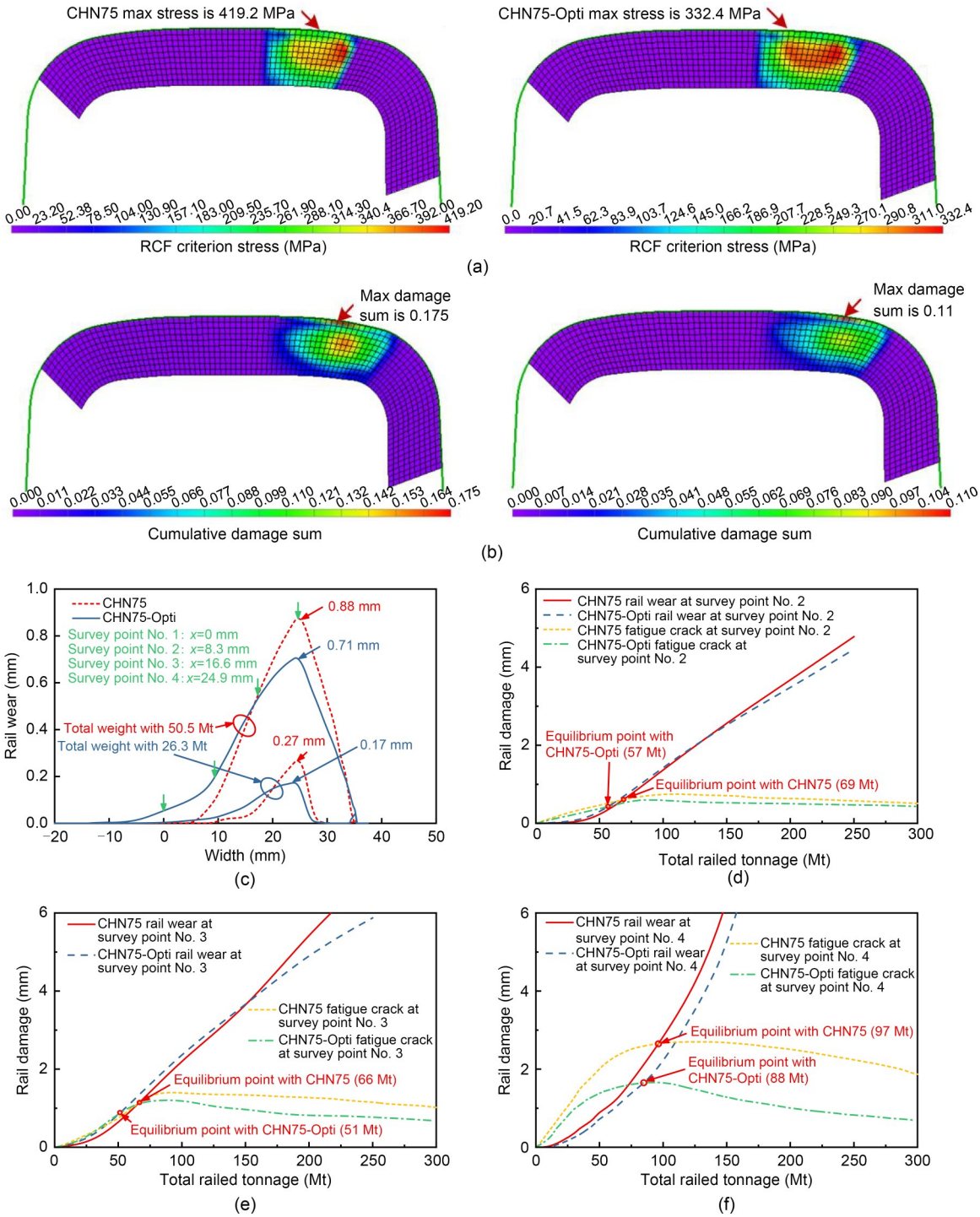

Fig. 10 Optimization results: (a) RCF criterion stress; (b) cumulative damage sum; (c) rail wear; (d) rail damage at survey point No. 2; (e) rail damage at survey point No. 3; (f) rail damage at survey point No. 4

wear of the rail. The CHN75-Opti rail increases the contact area between the wheel and rail, reducing the concentrated wear in the gauge angle region. For a total railed tonnage of 26.3 Mt, the maximum wear in the gauge angle decreases from 0.27 to 0.17 mm, and for a total railed tonnage of 50.5 Mt, the maximum wear reduces from 0.88 to 0.71 mm. Fig. 10d presents the fitting curve of wear damage at measuring point No. 2. On a 600 m curved track, the fatigue damage of the CHN75 rail is greater than the wear at 0 to 69 Mt;

the wear and fatigue then reach a balance at 69 Mt. Beyond this value, the wear damage surpasses fatigue damage.

With the implementation of the CHN75-Opti profile, the fatigue damage is also more significant than the wear damage when the weight is 0 to 57 Mt, and the balance between wear and fatigue is reached at 57 Mt. The optimization results in a 19% reduction in wear and a 16.8% decrease in fatigue cracks. Fig. 10e shows the fitting curve for wear and damage at measuring point No. 3. Similar to point No. 2, the balance for the CHN75 profile is reached at 66 Mt, while for the CHN75-Opti profile, it is achieved at 51 Mt. The optimization leads to a 22.8% decrease in wear and an 11.9% reduction in fatigue damage. Fig. 10f presents the fitting curve for wear and damage at measuring point No. 4. Consistent with the results at point No. 3, the balance for the CHN75 profile occurs at 97 Mt, while for the CHN75-Opti profile, it is achieved at 88 Mt. The optimization therefore results in a 22.5% reduction in wear and a 37.4% decrease in fatigue damage for this case.

The above results indicate that rail damage in a heavy-haul railway with a slight radius curve is a transitional process, from fatigue to wear. Our optimization method yielding the CHN75-Opti profile can effectively reduce the rail wear and rail fatigue damage and achieve a balanced relationship between wear and fatigue more quickly. However, this balance quickly disappears due to the rapid development of rail wear on small radius curves. Overall, the proposed optimization method effectively improves the contact relationship between the wheel and rail, significantly reducing fatigue and wear damage to the rail.

6 Conclusions

Since existing rail profile optimization methods have largely neglected the impact of rail fatigue, in this study, we adopted a combined approach of field testing and simulation analysis, and developed a rail profile optimization method that balances wheel-rail wear and fatigue.

After reconstructing a rail profile using NURBS curves, we used the coordinates of the rail profile value points as design variables. A numerical optimization model was then established using a PSO-LM-BP neural network, to reduce rail wear and fatigue damage as constrained by the geometric properties of the rail. An improved genetic algorithm leveraging chaotic microvariations was employed to achieve the solution, resulting in an optimized rail profile.

The static calculation results of the wheel-rail interface indicated that the optimized rail profile exhibits superior static performance. This was evidenced by a more uniform distribution of wheel-rail contact points, a larger contact patch area, a more stable difference in rolling circle radii, and equivalent conicity values.

The dynamic calculation results showed that the optimized rail profile demonstrates better dynamic performance. It was found that the optimized rail profile can reduce the maximum wheelset lateral force by 15%, the maximum derailment coefficient by 11%, the maximum wheel-rail contact stress by 10%, and the rail wear power by 26.6%.

Finally, it was demonstrated that using the CHN75-Opti profile along a R600 m curved section of heavy-haul rail lines can reduce rail-wheel contact stress, hasten the arrival of the wear and fatigue equilibrium state at measuring points Nos. 2−4, and decrease the wear rate by 22.5% and fatigue cracks by 37.4%, following the fatigue and wear equilibrium state being reached at measuring point No. 4.

Acknowledgments

This work is supported by the National Natural Science Foundation of China (No. 52388102) and the Sichuan Science and Technology Program (No. 2023ZDZX0008), China. The authors would like to thank the Guoneng Shuo-Huang Railway Development Company, China for providing vehicle parameters and line data for this project. The authors would also like to acknowledge the Xplorer Prize for sponsoring the project.

Author contributions

Binjie XU designed the research and wrote the first draft of the manuscript. Zhiyong SHI processed the corresponding data. Yun YANG helped to organize the manuscript. Jianxi WANG and Kaiyun WANG revised and edited the final version.

Conflict of interest

Binjie XU, Zhiyong SHI, Yun YANG, Jianxi WANG, and Kaiyun WANG declare that they have no conflict of interest.

References

Challen JM, Oxley PLB, Hockenhull BS, 1986. Prediction of Archard's wear coefficient for metallic sliding friction assuming a low cycle fatigue wear mechanism. *Wear*, 111(3):

275-288.
https://doi.org/10.1016/0043-1648(86)90188-2

Ding JJ, Sun SL, Li F, et al., 2012. Simulation of coupling relationship between wheel rolling contact fatigue and wear. *Journal of Mechanical Engineering*, 48(16):86-90.
https://doi.org/10.3901/JME.2012.16.086

Ekberg A, Marais J, 2000. Effects of imperfections on fatigue initiation in railway wheels. *Proceedings of the Institution of Mechanical Engineers, Part F: Journal of Rail and Rapid Transit*, 214(1):45-54.
https://doi.org/10.1243/0954409001531234

Evans JR, Lee TKY, Hon CC, 2008. Optimising the wheel/rail interface on a modern urban rail system. *Vehicle System Dynamics*, 46(sup1):119-127.
https://doi.org/10.1080/00423110701882355

Grassie S, Nilsson P, Bjurstrom K, et al., 2002. Alleviation of rolling contact fatigue on Sweden's heavy haul railway. *Wear*, 253(1-2):42-53.
https://doi.org/10.1016/S0043-1648(02)00081-9

Hiensch M, Burgelman N, 2019. Rolling contact fatigue: damage function development from two-disc test data. *Wear*, 430-431:376-382.
https://doi.org/10.1016/j.wear.2019.05.028

Hu YL, Ge X, Ling L, et al., 2025. Dynamic performance of a high-speed train exiting a tunnel under crosswinds. *Journal of Zhejiang University-SCIENCE A*, 26(1):21-35.
http://doi.org/10.1631/jzus.A2300610

Jendel T, 2002. Prediction of wheel profile wear—comparisons with field measurements. *Wear*, 253(1-2):89-99.
https://doi.org/10.1016/S0043-1648(02)00087-X

Kalousek J, Sroba P, Hegelund C, 1989. Analysis of rail grinding tests and implications for corrective and preventative grinding. The Fourth International Heavy Haul Railway Conference, p.193-204.

Kalker JJ, 1982. A fast algorithm for the simplified theory of rolling contact. *Vehicle System Dynamics*, 11(1):1-13.
https://doi.org/10.1080/00423118208968684

Kang SJ, Lee IS, Lee KH, et al., 2002. Hecke algebras, Specht modules and Gröbner–Shirshov bases. *Journal of Algebra*, 252(2):258-292.
https://doi.org/10.1016/S0021-8693(02)00071-6

Li YX, Dai LC, Guo ZT, et al., 2024. Carbody abnormal lateral vibration failure of high–speed train induced by the coupling factor of the wheel re-profiling method and excessive rail wear. *Engineering Failure Analysis*, 160:108170.
https://doi.org/10.1016/j.engfailanal.2024.108170

Lin FT, Hu WH, 2020. Study on the economical grinding surface of wear rail. *Journal of Railway Science and Engineering*, 17(10):2493-2502 (in Chinese).
https://doi.org/10.19713/j.cnki.43-1423/u.T20191152

Lin FT, Zhou S, Dong XQ, et al., 2021. Design method of LM thin flange wheel profile based on NURBS. *Vehicle System Dynamics*, 59(1):17-32.
https://doi.org/10.1080/00423114.2019.1657908

Magel EE, Kalousek J, 2002. The application of contact mechanics to rail profile design and rail grinding. *Wear*, 253(1-2):308-316.
https://doi.org/10.1016/S0043-1648(02)00123-0

Nikbakht S, Anitescu C, Rabczuk T, 2021. Optimizing the neural network hyperparameters utilizing genetic algorithm. *Journal of Zhejiang University-SCIENCE A*, 22(6):407-426.
https://doi.org/10.1631/jzus.A2000384

Ran L, Ding Y, Chen QZ, et al., 2023. Influence of adjacent shield tunneling construction on existing tunnel settlement: field monitoring and intelligent prediction. *Journal of Zhejiang University-SCIENCE A*, 24(12):1106-1119.
https://doi.org/10.1631/jzus.A2200573

Sun Y, Zhu SY, Zhai WM, 2018. Influence of tread hollow-worn wheel on wheel/rail interaction. *Journal of Mechanical Engineering*, 54(4):109-116.
https://doi.org/10.3901/JME.2018.04.109

Tian GR, Zhang WH, Chi MR, 2009. Study on curve negotiation performance of heavy-haul train. *Journal of the China Railway Society*, 31(4):98-103 (in Chinese).
https://doi.org/10.3969/j.issn.1001-8360.2009.04.017

Wang P, Gao L, 2015. Numerical simulation of wheel wear evolution for heavy haul railway. *Journal of Central South University*, 22(1):196-207.
https://doi.org/10.1007/s11771-015-2510-1

Wang JX, Chen X, Li XG, et al., 2015. Influence of heavy haul railway curve parameters on rail wear. *Engineering Failure Analysis*, 57:511-520.
https://doi.org/10.1016/j.engfailanal.2015.08.021

Wang WJ, Chen MT, Gu G, et al., 2007. Rail grinding technique and its application in high-speed railway. *Journal of Southwest Jiaotong University*, 42(5):574-577 (in Chinese).
https://doi.org/10.3969/j.issn.0258-2724.2007.05.011

Xie YL, Wang WJ, Guo J, et al., 2023. Rail rolling contact fatigue response diagram construction and shakedown map optimization. *Wear*, 528-529:204964.
https://doi.org/10.1016/j.wear.2023.204964

Xu X, Ding L, Miao HC, et al., 2023. Nonproportionally multiaxial cyclic plastic deformation of U75 rail steel: experiment and modeling. *International Journal of Fatigue*, 168:107480.
https://doi.org/10.1016/j.ijfatigue.2022.107480

Xu XN, Wen ZY, Ni Y, et al., 2024. Study on monitoring broken rails of heavy haul railway based on ultrasonic guided wave. *Scientific Reports*, 14(1):8667.
https://doi.org/10.1038/s41598-024-59328-5

Yang Y, 2019. Optimization of Rail Profile on Curve Based on the Competitive Relationship Between Fatigue and Wear. MS Thesis, Shijiazhuang Tiedao University, Shijiazhuang, China (in Chinese).

Yang Y, He QL, Cai CB, et al., 2024. A novel 3D train-bridge interaction model for monorail system considering nonlinear wheel-track slipping behavior. *Nonlinear Dynamics*, 112(5):3265-3310.
https://doi.org/10.1007/s11071-023-09240-w

You SY, Tang JY, Zhou W, et al., 2022. Research on calculation of contact fatigue life of rough tooth surface considering residual stress. *Engineering Failure Analysis*, 140:106459.
https://doi.org/10.1016/j.engfailanal.2022.106459

Zakharov SM, Goryacheva IG, 2005. Rolling contact fatigue

defects in freight car wheels. *Wear*, 258(7-8):1142-1147. https://doi.org/10.1016/j.wear.2004.03.062

Zakharov SM, Goryacheva I, Bogdanov V, et al., 2008. Problems with wheel and rail profiles selection and optimization. *Wear*, 265(9-10):1266-1272. https://doi.org/10.1016/j.wear.2008.03.026

Zhai WM, Gao JM, Liu PF, et al., 2014. Reducing rail side wear on heavy-haul railway curves based on wheel-rail dynamic interaction. *Vehicle System Dynamics*, 52(S1): 440-454. https://doi.org/10.1080/00423114.2014.906633.

Zhang CC, Zhou Y, Huang XW, et al., 2019. Research on the rail pre-grinding strategy and growth characteristics of rail defects in high-speed railway. *Journal of East China Jiaotong University*, 36(2):33-40 (in Chinese).

Zhao X, Wen ZF, Wang HY, et al., 2021. Research progress on wheel/rail rolling contact fatigue of rail transit in China. *Journal of Traffic and Transportation Engineering*, 21(1): 1-35. https://doi.org/10.19818/j.cnki.1671-1637.2021.01.001

Zhao Y, Nan J, Cui FY, et al., 2007. Water quality forecast through application of BP neural network at Yuqiao reservoir. *Journal of Zhejiang University-SCIENCE A*, 8(9): 1482-1487. https://doi.org/10.1631/jzus.2007.A1482

Zhou Y, Zhang J, Yang XW, et al., 2015. U75V Experiment on the rolling contact fatigue crack and wear of U75V heat-treated rail. *Journal of Tongji University*, 43(6):877-881 (in Chinese). https://doi.org/10.11908/j.0253-374x.2015.06.011

Zhou Y, Wang Z, Lu ZC, et al., 2021. Verification of prediction method for coexistence of rolling contact fatigue crack initiation and wear growth in rail. *Journal of Tongji University*, 49(3):411-420 (in Chinese). https://doi.org/10.11908/j.0253-374x.20402

Electronic supplementary materials

Sections S1–S9